Applied Catalysis B: Environmental 234 (2018) 56–69

Contents lists available at ScienceDirect

Applied Catalysis B: Environmental

journal homepage: www.elsevier.com/locate/apcatb

On the role of $BmimPF_6$ and P/F- containing additives in the sol-gel synthesis of TiO_2 photocatalysts with enhanced activity in the gas phase degradation of methyl ethyl ketone

Yige Yan*, Valérie Keller, Nicolas Keller*

Institut de Chimie et Procédés pour l'Energie, l'Environnement et la Santé (ICPEES), CNRS UMR 7515, University of Strasbourg, 25 rue Becquerel, 67087 Strasbourg Cedex, France

ARTICLE INFO

Keywords:
Photocatalysis
TiO_2 sol-gel synthesis
Ionic liquid
Synthesis mechanism

ABSTRACT

The role of phosphate and fluoride ions brought by the $BmimPF_6$ ionic liquid *via* hydrolysis during the sol gel synthesis of TiO_2 has been investigated by replacing $BmimPF_6$ with phosphorous- and fluorine-containing additives, phosphoric acid (PA) and sodium fluoride (NaF), respectively. Correlation between the physico-chemical properties and the photocatalytic behavior of the synthesized TiO_2 materials was established. High crystallinity anatase TiO_2 photocatalysts with controlled crystallite size and shape resulting from P/F-induced modifications displayed strongly improved photocatalytic activity and mineralization yield under UV-A illumination in the degradation of methyl ethyl ketone (MEK) taken as model Volatile Organic Compound (VOC), compared to the TiO_2 Aeroxide P25 reference and sol-gel TiO_2 counterpart synthesized in absence of any $BmimPF_6$. We showed that the $BmimPF_6$ ionic liquid could be efficiently substituted by cheap PA and NaF additives in an adequate ratio in the sol-gel synthesis for synthesizing TiO_2 photocatalysts without altering the main physico-chemical properties and the photocatalytic activity. We proposed a similar synthesis mechanism in both ionic liquid- and P/F-assisted sol-gel syntheses of TiO_2, involving a combined role of phosphate and fluoride ions. The reaction of phosphates with titanium hydroxide network in the early stage of the sol-gel synthesis resulted in a size control of TiO_2 crystallites and thus in higher specific surface area, in favor of a higher MEK conversion rate, while the fluoride ions were hypothesized to cause an anisotropic TiO_2 crystal growth during the aging step of the sol gel synthesis, in favor of a higher selectivity to CO_2 through a favored adsorption of intermediate products of MEK degradation on the exposed TiO_2 {001} facets.

1. Introduction

Heterogeneous photocatalysis on semi-conductor is a research field which gained importance over the last decades due to increasing challenges in environmental concerns and energy demands [1–3]. In the frame of the search for sustainable and green approaches, the photocatalytic oxidation has been shown to be promising for environmental reactions such as water detoxification or gaseous pollutant removal [4–7]. Among usually studied semi-conductors, the wide band-gap anatase TiO_2 still remains considered as the most efficient photocatalyst under UV-A illumination.

A variety of strategies have been implemented for enhancing the photocatalytic activity of TiO_2, and factors such as the surface area [8], the presence of bulk or surface defects [9], the type and density of surface chemical states [10,11] and furthermore the TiO_2 morphology [12], have been reported to affect the photocatalytic oxidation performances.

The simple, cost effective and versatile sol-gel synthesis method has already been largely applied for preparing with high synthesis yield, photocatalysts with controlled and tunable bulk and surface physico-chemical properties, including a high homogeneity, fine-scale and controllable morphology [13,14]. Applying controlled modifications of the synthesis parameters or adding additive compounds has been shown to allow especially a fine tuning of the catalyst morphology [15–19].

Room temperature ionic liquids (IL) are an exceptional type of chemical compounds which are composed nearly by only ions at room temperature. They take advantage of a negligible vapor pressure, a high chemical stability, non flammability properties and a recyclability for being considered and used as green solvents with tunable properties in reaction media for various synthesis and catalytic applications [20,21]. Most of the attractiveness of IL relates to the possibility to tune

* Corresponding authors.
E-mail addresses: yige.yan@etu.unistra.fr (Y. Yan), nkeller@unistra.fr (N. Keller).

https://doi.org/10.1016/j.apcatb.2018.04.027
Received 8 January 2018; Received in revised form 6 April 2018; Accepted 14 April 2018
Available online 16 April 2018
0926-3373/

Table 1
Influence of the presence of $BmimPF_6$ during the sol-gel TiO_2 synthesis on the BET specific surface area and the mean crystallite size of TiO_2 photocatalysts ($BmimPF_6$/Ti molar ratio of 0.03, aging duration of 18 h and 6 days).

Sample name	$BmimPF_6$/Ti molar ratio	P/Ti molar ratio		Aging duration	BET surface area (m^2/g)		Mean crystallite size (nm)[c]	
		bulk	surface		Dried samples	Calcined samples	Dried samples	Calcined samples [a]
P25	–	–	–	–	–	55 [a]	–	22[b]
IL0 6d	0	–	–	6 days	286	50	6	19
IL 18 h	0.03	0.01	n.m.[d]	18 h	294	110	7	10
IL 6d	0.03	0.01	0.06	6 days	251	97	8	11

[a] Aeroxide P25 TiO_2 was used as it.
[b] Corresponding to the TiO_2 anatase phase.
[c] The mean TiO_2 crystallite size, *i.e.* the average size of the coherent diffracting domains, was derived from XRD measurement through the Scherrer equation applied to the {101} peak at 25.7° with the usual assumption of spherical crystallites.
[d] not measureable.

properties by choosing their adequate cation/anion association [22].

IL received a growing interest in the field of inorganic chemistry, *e.g.* metal electro-deposition [23], ionothermal synthesis [24] and sol-gel chemistry. By acting as aging control agent, catalyst, co-solvent, or *via* an underrated nanostructure shaping ability resulting from their large size organic cation and from a non-coordination anion combination configuration, they can be used as structure-directing additives for synthesizing inorganic nanostructures [21,25]. They have recently attracted a significant interest as a new kind of template agent in various types of synthesis of TiO_2. Yoo et al. [26] have shown that the use of 1-Butyl-3-methylimidazolium hexafluorophosphate ($BmimPF_6$) can result in synthesizing smaller TiO_2 nanoparticles with a better crystallinity and a better thermal resistance. Although thermally stable mesoporous anatase TiO_2 nanoparticles with a high surface area and small size crystallites have been obtained *via* the participation of IL like $BmimPF_6$, the large amount of expensive IL required in the process (IL/Ti atomic ratio larger than 3) is a major economical drawback when compared to the use of conventional templating agents or surfactants. Choi *et al.* [27] were able to use 1/100 of the IL quantity used by Yoo et al., but both the BET surface and the photocatalytic activity were dramatically reduced.

To our knowledge, a detailed mechanism including the structuration role of the $BmimPF_6$ IL involved in sol-gel or solvothermal reactions was not described till now. Among scarce reports, Zhao et al. [28] have investigated the role of $BmimBF_4$ IL for obtaining shape-controlled TiO_2 crystals in a hydrothermal synthesis, and they have shown that both the fluorine and the $Bmim^+$ ions released from the ionic liquid played a role of capping agent and favor the {001} and {100} facet growth, respectively. But unfortunately the TiO_2 crystals were too large (crystal size diameter around 100–500 nm) for maintaining a high surface area, so that they might not be efficiently used in environmental depollution processes. Even if the capping mechanism of $BmimBF_4$ IL was well demonstrated, the same mechanism cannot be directly extrapolated to $BmimPF_6$, as PF_6^- differs from BF_4^- in many chemical properties [29]. So both the role played by $BmimPF_6$ and the detailed mechanism in the TiO_2 sol-gel synthesis still remain to be proposed.

In this work, shape- and size-engineered TiO_2 with highly crystallized nanoparticles and enhanced photocatalytic performances was firstly synthesized by a sol-gel route using a small amount of $BmimPF_6$. Further, the role played by $BmimPF_6$ – and especially that played by the phosphorus (P) and the fluorine (F) constituents – on the control of the TiO_2 properties was studied, by replacing $BmimPF_6$ by controlled combinations of the individual components of the ionic liquid. Gaseous butanone (methyl ethyl ketone, MEK), a typical malodorous pollutant of dwelling home indoor air whose presence results from its use as solvent in the production of many consumer products such as protective coatings and adhesives, glues, varnishes, plastics, textiles, paints or magnetic tapes, was taken as gas phase model VOC for assessing the photocatalytic activity of the TiO_2. Details on the mechanism of this well-documented photocatalytic degradation reaction can be found elsewhere [30–32]. Commercial Aeroxide® TiO_2 P25 from Evonik was used as reference TiO_2 powder. Correlation between the sol-gel synthesis mechanism involving IL and/or IL replacement additives, the physico-chemical properties of the synthesized photocatalyst and the photocatalytic activity under UV-A light was proposed.

2. Experimental

2.1. Catalyst preparation

2.1.1. Ionic liquid assisted sol-gel synthesis of TiO_2

In a typical ionic liquid assisted sol-gel synthesis, 5 g of titanium (IV) isopropoxide (TTiP, $Ti(O^iPr)_4$, 97%, Aldrich) was mixed in 10 g of propan-2-ol (AnalaR Normapur, > 99.5%, VWR Chemicals), before 0.09 g of $BmimPF_6$ ionic liquid (> 99%, Carl Roth) was added corresponding to a $BmimPF_6$/Ti molar ratio of 0.03. After stirring for 30 min, a $BmimPF_6$/alcohol two-phase mixture was formed since $BmimPF_6$ is not miscible with either TTiP or propan-2-ol. Then 6.2 g of 2.2 mol/L acetic acid solution as acid catalyst was further added dropwise. A white milky precipitate was formed immediately upon hydrolysis process and the solution was kept under stirring for 1 h, before being further sealed by parafilm and aged at room temperature for 18 h or 6 days without any stirring. After filtration of the powder from the rest of the solvent, the solid was dried for 2 h at 100 °C, and the light yellow powder obtained was washed under stirring in 100 mL acetonitrile overnight, dried overnight at 100 °C and further vacuum filtrated with 2 x 50 mL distilled water for 10 min, before being dried again for 2 h at 100 °C. The so-obtained white powder was finally calcined in air at 550 °C for 2 h with a heating rate of 5 °C/min in order to remove fluorine adsorbed on the sample surface [33]. Table 1 summarizes the labeling of TiO_2 samples.

For comparison, reference sol-gel TiO_2 was synthesized by following the same protocol in the absence of any $BmimPF_6$ IL.

2.1.2. Sol-gel synthesis of TiO_2 with ionic liquid replacement additives

The role of $Bmim^+$, phosphate anion, and fluoride anion - three constitutive components of the $BmimPF_6$ ionic liquid - was studied by replacing $BmimPF_6$ by two among three selected chemical compounds, namely 1-Butyl-3-methylimidazolium chloride (BmimCl (BC), ≥95%, Aldrich), sodium fluoride (NaF, ACS reagent, ≥99%, Sigma-Aldrich) and phosphoric acid (H_3PO_4 (PA), analytical reagent, ≥85%, R.P.Normapur). They provided to the synthesis media the $Bmim^+$ cation, the fluoride anion (F^-) and the phosphate anions, respectively. The molar ratio of each additive to titanium was fixed at 0.03, similarly to the IL/Ti ratio.

Two aging durations were applied, *i.e.* 18 h and 6 days, and the calcination temperature was fixed at 550 °C, while the other parameters as well as the synthesis protocol were identical to those used in the

$BmimPF_6$-assisted TiO_2 sol-gel synthesis. Depending on the two additives selected in each combination and on the aging duration, the TiO_2 samples were labeled as BCPA 18 h, BCPA 6d, BCNaF 18 h, BCNaF 6d, PANaF 18 h and PANaF 6d.

2.2. Characterization methods

The P/Ti bulk atomic ratio of the TiO_2 samples was obtained by Inductively Coupled Plasma - Atomic Emission Spectroscopy (ICP-AES) performed at IPHC (Strasbourg, France). The X-ray diffraction (XRD) patterns of the samples were recorded on a D8 Advance Brucker powder diffractometer in a θ/θ mode and using the $K\alpha_1$ radiation of Cu at 1.5406 Å. The surface area measurements were carried out on an ASAP2010 Micromeritics Tristar 3000 analyser using N_2 as adsorbent at 77 K. X-ray photoelectron spectroscopy (XPS) characterization was performed on a Thermo VG Scientific equipped with X-Ray source of Al K_α radiation (hv = 1486.6 eV). Transmission Electron Microscopy (TEM) analysis was performed using a Philips CM200 in standard mode observation, equipped with thermo-ionic LaB_6 filament, operating at a 200 kV acceleration voltage. Details on the characterization devices can be found as SI 1.

2.3. Gas-phase photocatalytic tests

The photocatalytic performance and behavior of TiO_2 samples are assessed by their ability to degrade and mineralize MEK under UV-A irradiation in a single-pass continuous gas flow reactor, with a flat configuration derived from that detailed in the ISO 22197 standard series [34] (Fig. SI 2).

50 mg of TiO_2 powder, corresponding to a surface density of 1 $mg.cm^{-2}$, was evenly coated by adding drop-wisely onto a glass plate (100 mm length, 50 mm width and 3 mm thickness for fitting into the reactor) and simultaneously evaporating a TiO_2 ethanoic suspension to dryness. Prior to that, the suspension was stirred overnight and sonicated for 30 min. Finally, the TiO_2-coated glass plate was dried overnight at 100 °C. This TiO_2 surface density was previously determined as being adequate for evaluating the activity of photocatalysts in such operating conditions [35].

Two synthetic air flows were bubbled at ambient temperature and atmospheric pressure through two temperature-controlled saturators containing MEK (butan-2-one, Sigma-Aldrich, > 99%) and distilled water, respectively, and mixed with an additional synthetic air flow to set an inlet MEK concentration at 100 ppm_v, relative humidity (RH) at 50% and a total air flow rate at 227 ml/min, corresponding to a velocity of 1.33 cm/s^{-1} and a residence time of 7.5 s in the reaction zone of the reactor. A test temperature of 25 °C was maintained throughout the test.

The photocatalytic performances were obtained by *on-line* quantifying both inlet and outlet flows using a R3000A gas micro-chromatography (SRA instruments), equipped with thermal conductivity micro-detectors, allowing quantification of MEK, water, CO_2 and acetaldehyde.

The photocatalysts were firstly exposed for 2 h to the inlet polluted air flow with no illumination until dark adsorption equilibrium was reached, before the UV−A illumination was switched on. The UV−A illumination was provided by a 8 W UV−A blacklight lamp (Sylvania Blacklight Blue F8W/BLB T5), with a spectral peak centered on 365 nm, so that the photo-catalytic material was exposed to an irradiance of 3.0 $mW.cm^{-2}$, as recorded using a wideband spectroradiometer (RPS900-W ILT). The catalytic activity was evaluated under steady state conditions, typically achieved after 3 h of irradiation. No change in activity was observed for all samples for 24 h after reaching steady state conditions. The absence of any deactivation during the MEK oxidation allowed the TiO_2 photocatalysts to be re-used if necessary.

The photocatalytic activity was expressed in terms of MEK conversion (C_{MEK}), of selectivities to acetaldehyde (S_{Ac}) and CO_2 (S_{CO_2}), as main reaction intermediate byproduct and final oxidation product, respectively, as well as of CO_2 mineralization yield (Y_{CO_2}), calculated according to Eqs. (1)–(4):

$$C_{MEK}(\%) = \frac{([MEK_{in}]-[MEK_{out}])}{[MEK_{in}]} * 100 \quad (1)$$

$$S_{Ac}(\%) = \frac{[Ac_{out}]}{([MEK_{in}]-[MEK_{out}])* 2} * 100 \quad (2)$$

$$S_{CO_2}(\%) = \frac{[CO_{2\,out}]}{([MEK_{in}]-[MEK_{out}])* 4} * 100 \quad (3)$$

$$Y_{CO_2}(\%) = \frac{[CO_{2\,out}]}{[MEK_{in}]* 4} * 100 \quad (4)$$

All the photocatalytic tests have been performed twice, and the photocatalytic data corresponded to the averaged data, with a relative accuracy of ± 5%.

3. Characterization of photocatalysts

3.1. TiO_2 synthesized via $BmimPF_6$ IL assistance

3.1.1. Structural properties

The XRD patterns of the IL-derived TiO_2 samples are shown in Fig. 1. Their main bulk physico-chemical properties such as the mean crystallite sizes derived from XRD measurements and the specific surface areas are reported in Table 1. XRD patterns show only anatase phase as crystalline phase, with or without addition of $BmimPF_6$, and

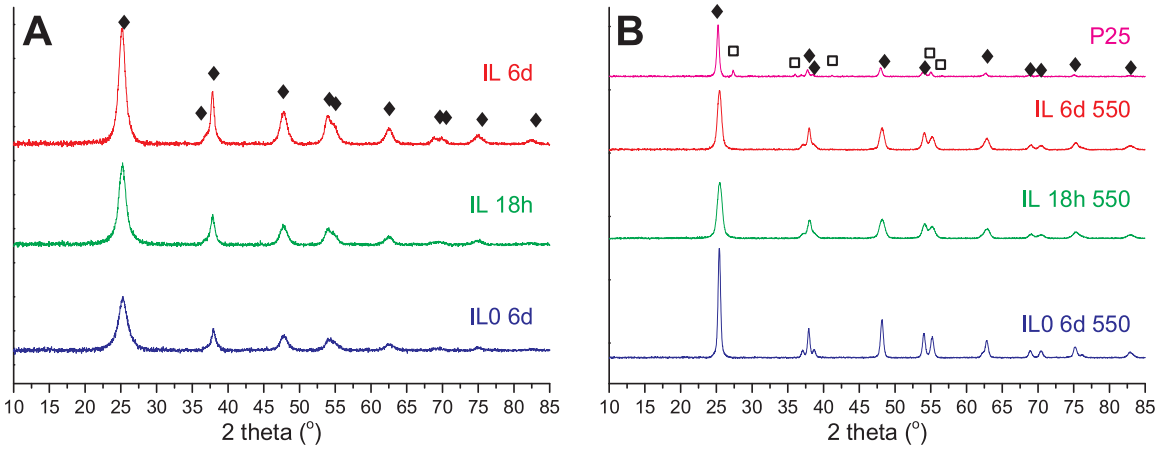

Fig. 1. XRD patterns of TiO_2 IL0 6d, IL 18 h and IL 6d samples, (A) after the drying step and (B) after calcination at 550 °C. TiO_2 P25 is compared as reference. Black diamonds are anatase peaks, hollow cubes are rutile peaks.

whether the samples were calcined at 550 °C or only dried at 100 °C.

The dried sample after 6 days of aging synthesized without $BmimPF_6$ already showed the presence of partially crystallized anatase TiO_2 phase with a small mean crystallite size of 6 nm. However, the presence of $BmimPF_6$ favored the crystallization of TiO_2 during the aging step, while the mean crystallite size was slightly increased, from 6 nm for the reference sol-gel TiO_2 sample to 7–8 nm when TiO_2 was synthesized in the presence of $BmimPF_6$.

After calcination at 550 °C, the crystallinity of the sol-gel TiO_2 sample synthesized in the absence of $BmimPF_6$ strongly increased, together with a large increase of the mean crystallite size to 19 nm, close to that of 22 nm shown by the anatase phase in TiO_2 P25. By contrast, only a moderate increase in the mean crystallite size of TiO_2 synthesized in the presence of $BmimPF_6$, from 7 to 8 nm to 10-11 nm, was observed after 6 days of aging, whatever the aging duration. The presence of $BmimPF_6$ provided to the materials thermal resistance and the crystal growth during the calcination was hindered.

The TiO_2 materials displayed a bulk P/Ti molar ratio of 0.01, lower than the P/Ti ratio of the precursor mixture. After calcination of TiO_2 samples at 550 °C, no residual fluorine was detected by high pressure ion chromatography, in agreement with Jung *et al* [33]. Adsorbed fluorine has to be removed to avoid passivation of the photocatalyst surface before use [33,36].

Whether ionic liquid was involved or not in the synthesis, all anatase TiO_2 samples displayed after calcination a band gap energy of 3.2 ± 0.1 eV derived from the Diffuse Reflectance UV–vis spectra, similar to that of the TiO_2 P25 reference (not shown).

3.1.2. Surface area and porosimetry properties

Whether $BmimPF_6$ was used or not, dried TiO_2 displayed a high and non-microporous surface area within the 251-294 m^2/g range, resulting from a small mean crystallite size. The specific surface area of the reference sol-gel TiO_2 was drastically decreased after calcination down to 50 m^2/g, close to that of the TiO_2 P25 reference, as a result from similar mean crystallite sizes. By contrast, when $BmimPF_6$ was used, TiO_2 showed a different behavior, and calcined TiO_2 samples were able to maintain a high non-microporous specific surface area of 97-110 m^2/g, despite the use of a high calcination temperature.

The influence of the presence of $BmimPF_6$, of the aging duration and of the calcination on the N_2 sorption isotherms and the pore size distribution of TiO_2 are shown in Fig. 2. When $BmimPF_6$ was used, the presence of mesopores within the materials is suggested by the presence of mainly type-IV isotherms. Also, H_2-type of hysteresis was observed, corresponding to interconnected mesopores, with non-uniform size or shape. This differs from the isotherm obtained on the non-porous TiO_2 P25. When synthesized in the absence of $BmimPF_6$, dried TiO_2 displayed an isotherm with a H_3-type hysteresis, characteristic of aggregates or agglomerates of particles forming slit shaped pores with non-uniform size and/or shape, whereas the calcination at 550 °C resulted in the appearance of a H_1-type contribution, corresponding to the formation of more uniform and larger mesopores with a monomodal distribution centered on 15 nm. By contrast, when $BmimPF_6$ was used, the H_2-type hysteresis was mainly turned into a H_1-type hysteresis after calcination, with a monomodal pore size distribution centered on about 10 nm. Here, the presence of $BmimPF_6$ ionic liquid during the synthesis and aging seems to be a key factor for controlling the pore size and the surface area.

3.1.3. Morphological characterization

TEM images of Fig. 3 show the influence of the presence of $BmimPF_6$ on the TiO_2 nanocrystal morphology after 6 days of aging and calcination at 550 °C, and TiO_2 P25. The mean crystal size of the reference sol-gel TiO_2 was around 20 nm, similar to that of TiO_2 P25, but with a moderately homogeneous distribution. This crystal size distribution heterogeneity could result from a fast crystal growth during the calcination step. By contrast, the TiO_2 sample prepared with $BmimPF_6$ (Fig. 3c,d) displayed a smaller average crystal size with a more homogeneous distribution (Fig. 3b), in agreement with the XRD analysis.

In addition, the use of $BmimPF_6$ also led to a unique shape evolution with the aging time. The nanoparticle morphology turned from a round-like shape to a more square-like and faceted shape when increasing the aging duration from 18 h to 6 days (Fig. 3d), while maintaining constant the mean crystallite size. This shape change could result from the better crystallinity achieved after a longer aging step, or from the capping ability of F^- present in the synthesis medium. This capping ability associated with TiO_2 crystallization has been reported using hydrofluoric acid [37,38] or F-containing ionic liquid such as $BmimBF_4$ [28] as additive, although no sol-gel synthesis was concerned. Since the hexafluorophosphate anion of $BmimPF_6$ is the only F source in the synthesis, the involvement of $BmimPF_6$ in the aging duration-dependent crystal growth control, especially *via* the F^-, will be further investigated.

3.1.4. Surface analysis

Fig. 4 shows the XPS spectra of Ti_{2p}, O_{1s}, P_{2p} and F_{1s} orbital regions recorded on dried and calcined TiO_2 samples. Whether $BmimPF_6$ was used or not, and whether the TiO_2 sample was dried or calcined, the Ti_{2p} region pattern shows the typical Ti $2p^{3/2}$-Ti $2p^{1/2}$ doublet located at 458.3 eV and 464.0 eV with a spin-orbit coupling constant of 5.7 eV, and assigned to Ti^{4+} (Ti-O) in an octahedral in typical TiO_2 crystalline structure. No higher energy contribution that could be attributed to tetrahedral Ti-O-P bonds [39,40] was observed. Similarly, the O_{1s} spectra showed usual contributions from TiO_2 lattice O^{2-} in O-Ti bond and O—H surface groups, at 529.2 eV and 531.2 eV, respectively. The OH content was strongly reduced after calcination, in agreement with the decreasing surface area.

For dried TiO_2, the P_{2p} spectra did not reveal any P contributions. By contrast, the P_{2p} spectra of IL 6d 550 TiO_2 showed unambiguously the presence of P, with a P $2p^{3/2}$-P $2p^{1/2}$ doublet at 132.9 and 133.8 eV (with a spin-orbit coupling constant of 0.87 eV), characteristic of P in a pentavalent oxidation state (P^{5+}), and usually attributed to phosphate groups [41–43]. The P/Ti surface atomic ratio was calculated at 0.06. Before calcination, the phosphates were probably finely dispersed within the TiO_2 bulk, so that its surface content remained very low. The calcination at 550 °C could cause partial migration of phosphates species from the bulk to the surface, with consequently an increase in the P/Ti surface atomic ratio to a level overcoming that of the bulk, and observable by XPS. This was in agreement with the migration of phosphorous to the TiO_2 surface observed by Elghniji et al. for temperatures higher than 550 °C [44]. However, the presence of P as Ti-O-P bond contribution at higher binding energy was not observed on the Ti_{2p} spectra, like for the uncalcined samples, possibly due to the low content of P in TiO_2 samples.

No trace of residual nitrogen from $Bmim^+$ was observed in the dried or calcined TiO_2 samples, confirming the efficiency of the acetonitrile/water washing procedure for the cationic part of $BmimPF_6$. By contrast, residual F has been detected for the dried sample, with F_{1s} orbital peak at 683.3 eV. This may consist in F adsorbed on the material surface rather than in F incorporated in the TiO_2 host as substituent of O^{2-}, for which the F-Ti-O contribution at 688.3 eV was never observed whatever the TiO_2 samples [45]. This residual content diminished strongly after calcination, with a F/Ti surface atomic ratio decreasing from 0.18 to below the detection limit. This confirmed the full desorption of residual F from the TiO_2 surface during the calcination step at 550 °C [33].

3.2. TiO_2 synthesized with IL replacement additives

3.2.1. Structure properties

The XRD patterns of the dried and calcined TiO_2 samples synthesized with replacement additives are reported in Fig. 5 and their main bulk physico-chemical properties are reported in Table 2. Firstly,

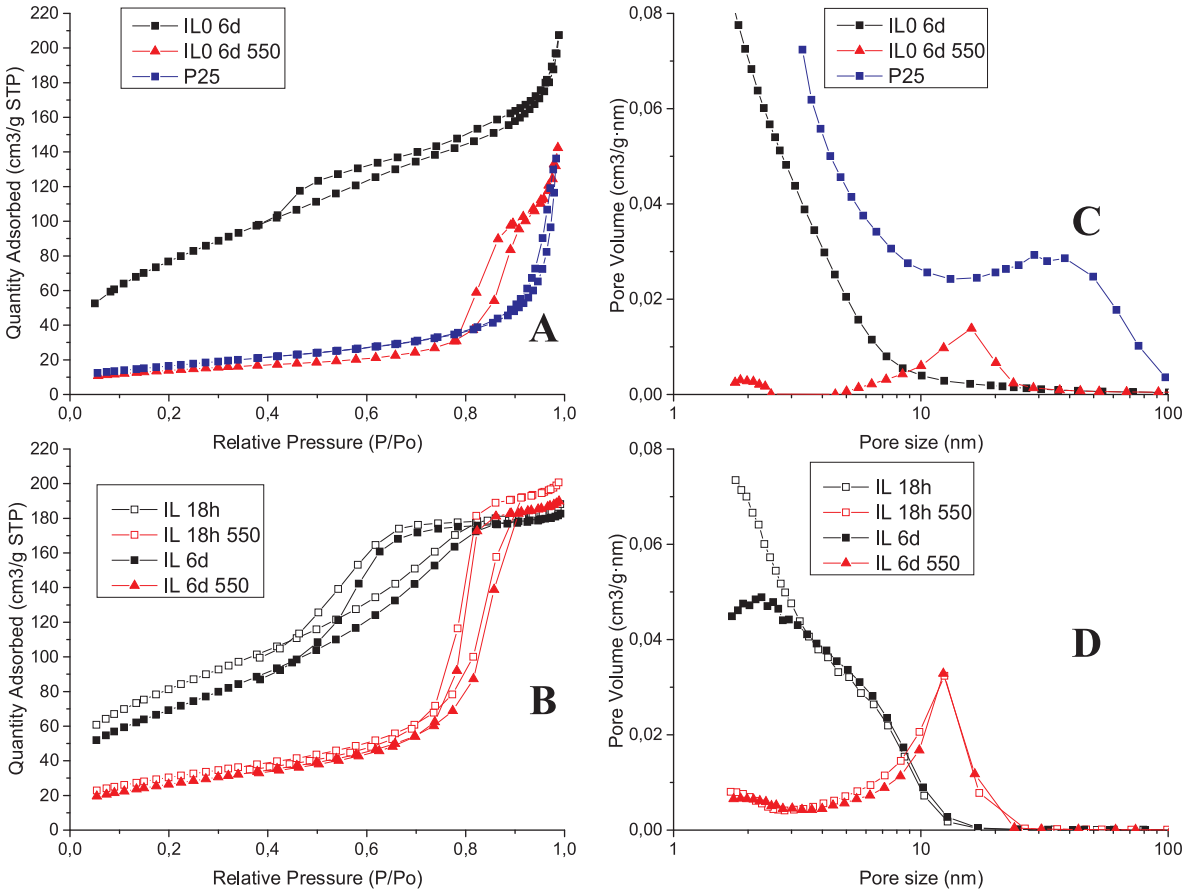

Fig. 2. N_2 adsorption/desorption isotherms and pore size distribution of dried and calcined TiO_2 materials synthesized with aging durations ranging from 18 h to 6 days, (A,C) without $BmimPF_6$, (B,D) with a $BmimPF_6$/Ti ratio of 0.03. Aeroxide TiO_2 P25 is shown as reference in (A, C).

whatever the replacement additive combination and the aging duration, only anatase was observed as crystallized phase in dried and calcined materials. Only samples prepared with P-containing additives, *i.e.* BCPA and PANaF samples, have shown an inhibition effect of the crystallite size growth during the calcination. Those samples maintained after calcination a relatively small mean crystallite size, around

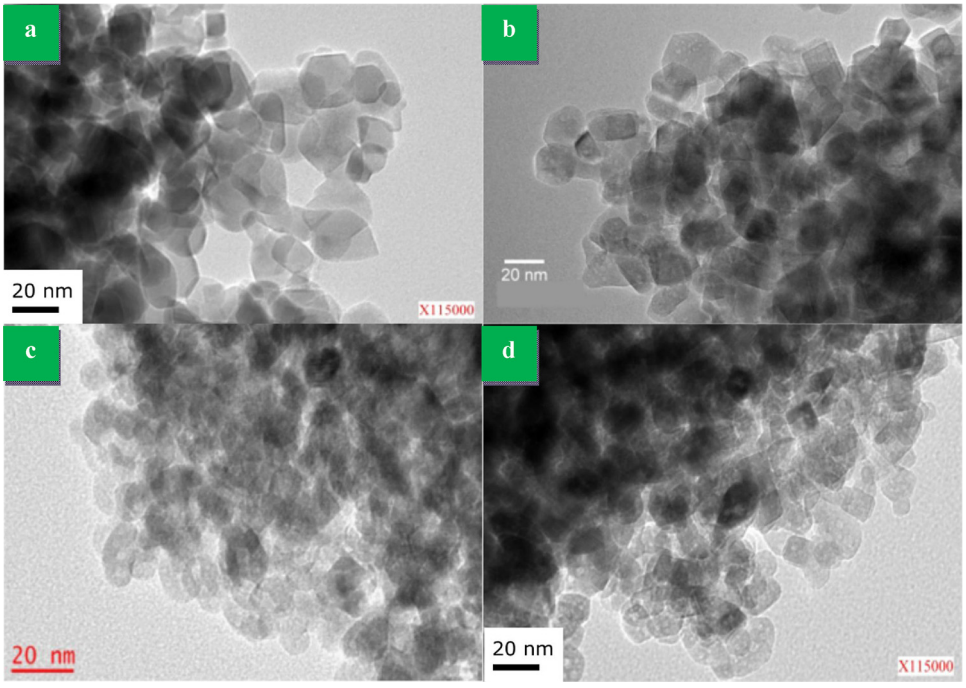

Fig. 3. TEM images of (a) TiO_2 P25, (b) IL0 550, (c) IL 18 h 550 and (d) IL 6d 550 (d).

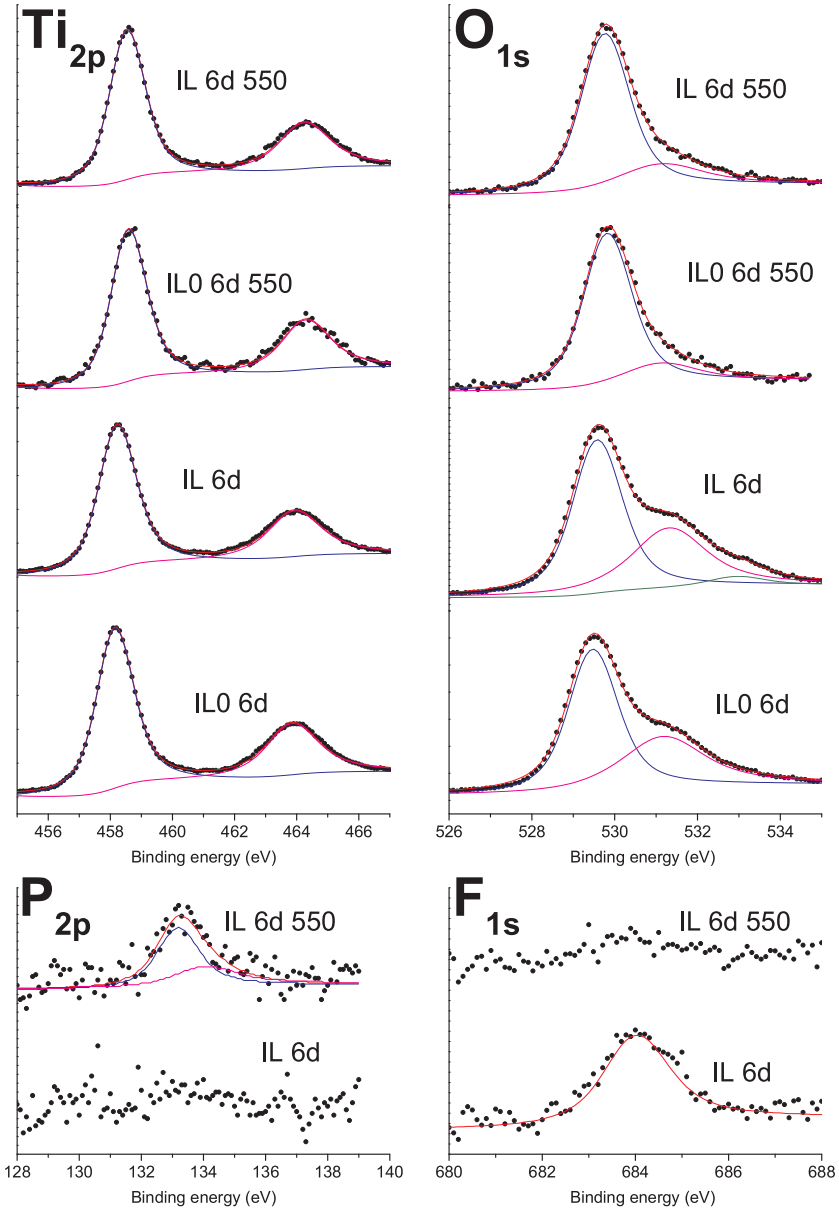

Fig. 4. Ti_{2p}, O_{1s}, P_{2p} and F_{1s} XPS patterns of dried and calcined IL0 6d and IL 6d TiO_2 samples.

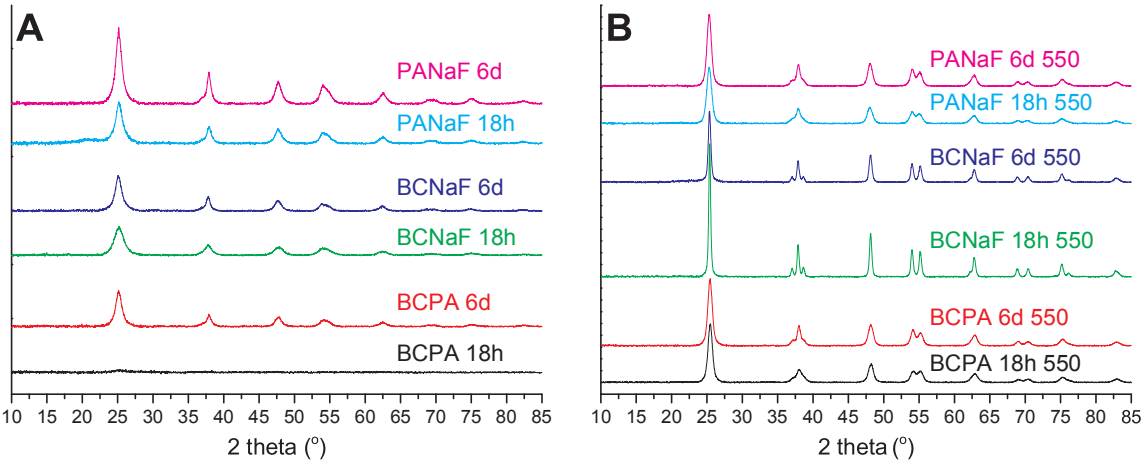

Fig. 5. XRD patterns of TiO_2 synthesized with replacement additives in the assisted sol-gel route : BCPA 18 h (black); BCPA 6d (red); BCNaF 18 h (green); BCNaF 6d (blue); PANaF 18 h (cyan); PANaF 6d (pink). (A) dried TiO_2 and (B) after calcination at 550 °C (For interpretation of the references to colour in this figure legend, the reader is referred to the web version of this article).

Table 2
Specific surface areas and mean crystallite sizes of TiO_2 samples synthesized by combination of replacement additives for $BmimPF_6$, in the assisted sol-gel route. The two replacement additives in one set of combination for each synthesis shared same molar ratio to Ti.

Sample name	Aging duration	BET surface area (m^2/g)	Mean crystallite size (nm) (Mean crystallite size before calcination)
BCNaF 18 h 550	18 h	31	24 (5)
BCNaF 6d 550	6 days	46	19 (8)
BCPA 18 h 550	18 h	91	11 (-[a])
BCPA 6d 550	6 days	109	10 (8)
PANaF 18 h 550	18 h	108	10 (8)
PANaF 6d 550	6 days	131	11 (8)

[a] Not measureable.

10–11 nm *vs* 8 nm for the dried samples, associated to a high surface area within the 90-130 m^2/g range. By contrast, the P-free BCNaF TiO_2 sample had a strong mean crystallite size increase after calcination, whatever the aging duration, from 5 and 8 nm before calcination to 24 and 19 nm after calcination. This was correlated to a medium surface area of 31 and 46 m^2/g, respectively. Also, the use of P-containing additives resulted in a better crystallinity of dried TiO_2 samples after the aging step than TiO_2 samples aged in the absence of any phosphorous. Interestingly, these characteristics are similar to those brought by $BmimPF_6$.

Whatever the IL replacement additives used in the synthesis, all anatase TiO_2 samples displayed after calcination a band gap energy of 3.2 ± 0.1 eV, similar to that obtained when using ILs in the synthesis (not shown).

3.2.2. Surface analysis

XPS analysis has been performed on both P-containing BCPA-, and PANaF-derived TiO_2 samples (Fig. 6 and Fig. SI 3). The TiO_2 sample prepared with BCNaF are not reported here. The spectra of Ti_{2p}, and O_{1s} orbitals for dried and calcined TiO_2 did not show any strong differences compared to those recorded on TiO_2 synthesized with $BmimPF_6$ (Fig. SI 3). By contrast, in BCPA- and PANaF-derived TiO_2 samples, the presence of P has been confirmed in dried and calcined TiO_2 (Fig. 6), with the characteristic doublet of $P_{2p}3/2$-$P_{2p}1/2$ orbitals corresponding to P—O bond in non-polymerized phosphates, at 132.9/133.8 eV (BCPA dried), at 133.2/134.1 eV (BCPA calcined), at 132.9/133.8 eV (PANaF dried) and at 133.3/134.2 eV (PANaF calcined). The P/Ti surface atomic ratio increased after calcination from 0.05 to 0.1 and from 0.06 to 0.09 for the BCPA- and PANaF-derived TiO_2 samples, respectively. The increase in the P/Ti surface ratio after calcination till a value overcoming that of the bulk measured at 0.01 for PA-derived samples, could result from a phosphate migration from the bulk to the surface, like it was proposed for TiO_2 synthesized in the presence of $BmimPF_6$.

3.2.3. Morphological characterization

The role of P in limiting the crystal size during calcination was also visualized in TEM by comparing TiO_2 materials prepared with and without P-containing additives, *i.e.* PANaF and BCNaF (Fig. 7), for which mean crystallite sizes around 12–15 nm and 22-25 nm, respectively, were observed, in agreement with the behavior observed by XRD.

4. Photocatalytic activity

4.1. TiO_2 synthesized via $BmimPF_6$ IL assistance

Firstly, no MEK oxidation occurred neither with the sole UV-A irradiation in the absence of TiO_2, nor in the presence of TiO_2 in the dark. The MEK conversion, the selectivities to acetaldehyde and CO_2, as well as the CO_2 mineralization yield achieved on calcined TiO_2 synthesized in the presence of $BmimPF_6$ and with an aging duration of 18 h and 6 days are shown in Table 3. The performances were compared to those achieved with TiO_2 P25 and with the reference sol-gel TiO_2, *i.e.* TiO_2 synthesized in the absence of $BmimPF_6$.

The reference TiO_2 P25 showed a MEK conversion of 37% with selectivities to CO_2 and acetaldehyde of 36% and 34% respectively, resulting in a CO_2 mineralization yield of 13%. It had a slightly higher activity than the reference sol-gel TiO_2 that achieved a MEK conversion of 32%, with a CO_2 mineralization yield of 10%. Considering that both materials have similar main characteristics in terms of specific surface area, crystallite size and crystallinity, the presence of anatase-rutile phase mixture in the TiO_2 P25 reference could be put forward for explaining the slight superiority of the P25 photocatalyst [46], although we know that the literature can be controversial when explaining the activity of the commercial P25.

By contrast, TiO_2 synthesized in the presence of $BmimPF_6$ showed a higher activity in terms of MEK conversion and CO_2 mineralization yield compared to both TiO_2 P25 and reference sol-gel TiO_2, with conversions of 48–50%, and CO_2 mineralization yields of 17% and 25%. 6 days of aging led to a higher CO_2 selectivity of 52% compared to that achieved on both the same sample aged for 18 h, similar to that achieved with the reference sol-gel TiO_2.

Also, dried TiO_2 synthesized in the presence of $BmimPF_6$ showed increased crystallinity, close to that of calcined samples, yet, no activity has been noticed. Passivation of the catalyst by fluorine in such small amount is unlikely a factor here. The absence of activity probably resulted from the presence of amorphous TiO_2 phases remaining within the catalysts (Fig. SI 4).

Whatever the TiO_2 samples, the carbon balance was not closed by MEK, CO_2 and acetaldehyde as the main reaction intermediate (Table SI 5). As reported in the literature, the carbon balance was probably

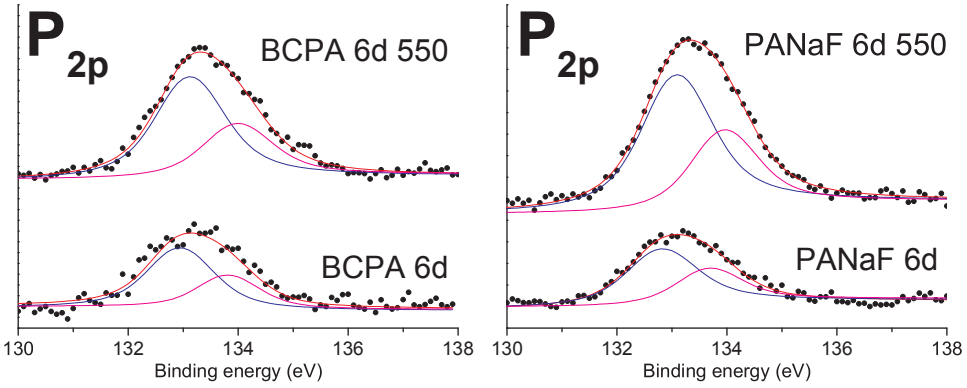

Fig. 6. P_{2p} XPS patterns of BCPA 6d, BCPA 6d 550, PANaF 6d and PANaF 6d 550.

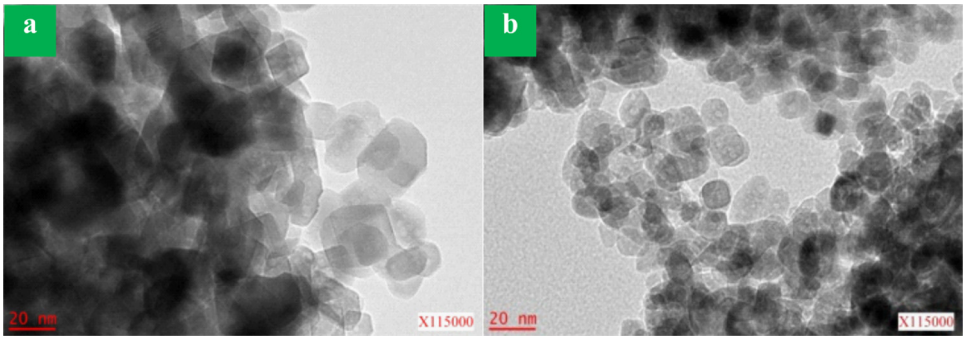

Fig. 7. TEM images of (a) BCNaF 6d 550 and (b) PANaF 6d 550.

Table 3
Results of the gas-phase photocatalytic degradation of MEK for calcined TiO_2 synthesized with $BmimPF_6$ and replacement additives. The corresponding specific surface areas are also reported.

Sample name	Aging duration	BET surface area (m^2/g)	MEK conversion (%)	CO_2 selectivity (%)	Acetaldehyde selectivity (%)	CO_2 mineralization yield (%)
P25	–	55	37	34	36	13
IL0 6d 550	6 days	50	32	30	25	10
IL 18 h 550	18 h	110	50	34	31	17
IL 6d 550	6 days	97	48	52	30	25
BCPA 6d 550	6 days	109	52	41	26	22
BCNaF 6d 550	6 days	46	31	42	28	13
PANaF 18 h 550	18 h	108	56	41	23	23
PANaF 6d 550	6 days	131	53	54	9	28

closed by other reaction intermediates, that could not be detected due to their small quantities or to the sensitivity of the analytical system [30–32,45].

4.2. TiO_2 synthesized with IL replacement additives

The results of the gas-phase photocatalytic degradation of MEK for calcined TiO_2 materials synthesized in the presence of two additives among BC, PA and NaF, are shown in Table 3.

The P-containing "BCPA 6d 550″ and “PANaF 6d 550″ photocatalysts exhibited a high MEK conversion of 52% and 53%, respectively, whereas the P-free “BCNaF 6d 550″ counterpart showed a lowest MEK conversion of 31%. In addition to a high MEK conversion, the PANaF 6d 550 TiO_2 led to a high CO_2 selectivity of 54% (with a low acetaldehyde selectivity of 9%, resulting in a high mineralization yield of 28%), when compared to the lower CO_2 selectivity and to the higher acetaldehyde selectivity achieved on the high MEK conversion BCPA counterpart (42% and 28%, respectively). Similarly to TiO_2 synthesized in the presence of $BmimPF_6$, the increase in the aging duration from 18 h to 6 days resulted in an increase in the CO_2 selectivity from 41% to 54% for the PANaF sample.

The morphological analysis of PANaF 6d dried sample provided by TEM images in Fig. 8 showed an anisotropic spindle-like morphology for the crystals. This morphology could derive from the capping ability of F^- anions present in the reaction medium during aging, since neither Na^+ nor PA is known for inducing a shape modification effect for TiO_2 crystals in solution. Discussion on the capping ability of F^- during the synthesis of TiO_2 samples will be made in relationship with the activity of the photocatalysts.

Here, the results obtained did not allow us to evidence a possible direct role of $Bmim^+$ on the photocatalytic activity of TiO_2 after calcination.

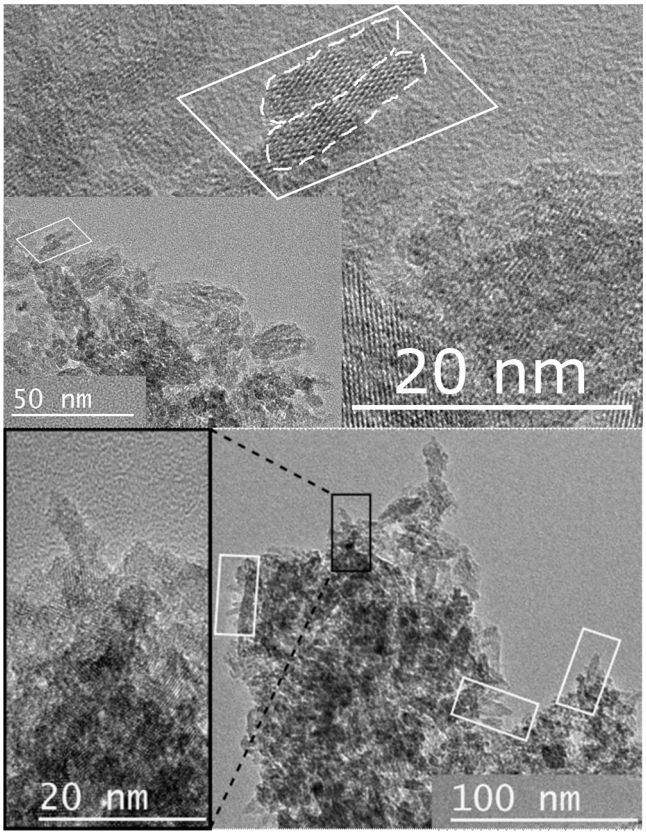

Fig. 8. TEM images of the dried PANaF 6d TiO_2 sample (after 6 days of aging). The aggregation of two crystallites is shown.

4.3. Correlation between IL-, P-, F- derived TiO_2 properties and photocatalytic activity

Whether $BmimPF_6$- or P-containing additives were involved, the increase in the surface area (and inversely the decrease in the mean crystallite size) of TiO_2 photocatalysts was strongly beneficial to the improvement of the MEK conversion. Also, the photocatalytic activity of $BmimPF_6$- and P-derived TiO_2 samples displayed a similar aging

duration-dependency. At a similar MEK conversion level, an increase in the CO_2 selectivity and in the CO_2 mineralization yield was observed for both TiO_2 sample series when the aging duration was increased. Since the samples displayed approximatively a similar surface area and a similar mean crystallite size, this dependency might be rather related to the morphology change of TiO_2 crystals during aging.

Despite a decrease in the isoelectric point from 6 to 3.5 has been observed with the incorporation of phosphate in TiO_2 samples (TiO_2 *vs.* IL-TiO_2 and PA-TiO_2), no significant change in the adsorption behavior was observed during the adsorption period, except a slight increase in the amount of MEK and H_2O adsorbed at the dark adsorption equilibrium, that was directly related to the increase in the TiO_2 surface area.

The performances shown by the "PANaF 6d 550″ photocatalyst were not only the highest observed among the TiO_2 photocatalysts synthesized with the use of $BmimPF_6$ replacement additives, but also they were slightly superior to those achieved over the most active TiO_2 photocatalyst synthesized with $BmimPF_6$. So, the high photocatalytic activity of TiO_2 samples might result from the presence of P and F elements in $BmimPF_6$ and only the combined influence of those two elements might result in a comparable or even higher photocatalytic activity than that obtained on TiO_2 synthesized in the presence of $BmimPF_6$. This enhancement of the photocatalytic activity could be related to the beneficial TiO_2 physico-chemical properties evolution reported early, through a room-temperature crystallization mechanism during the aging in presence of P and F elements.

5. Discussion

P and F are hypothesized to be the two elements in $BmimPF_6$ and in additives playing a key-role in the sol-gel synthesis of TiO_2 nanomaterials. We have noticed three major impacts of their presence in the synthesis media that influenced the physico-chemical properties of TiO_2 and affected the photocatalytic behavior. The activity of TiO_2 photocatalysts:

- showed an aging-duration dependency.
- was influenced by a F-induced modification of the crystal shape, especially the CO_2 selectivity.
- showed a dependency with a P-induced size modification, especially the MEK conversion.

5.1. Room temperature aging effect

Surface area and XRD analyses indicated together an aging duration-dependent crystal size evolution in the TiO_2 sol-gel synthesis at room-temperature. We assumed that this resulted from a room temperature self-crystallization process of TiO_2 in solution during the aging step. Conventionally, most of the crystallization processes of TiO_2 materials from amorphous to anatase were achieved and studied in high-pressure and high-temperature hydrothermal conditions, although studies have reported possible low-temperature sol-gel approaches for synthesizing anatase crystals by aging the sol [47,48]. In one recent review about crystal growth of inorganic functional materials, Zhang et al. stated that the classical growth of crystals occurs through atom-by-atom or monomer-by-monomer addition to an inorganic or organic template, or through the dissolution of unstable phases (small particles or metastable polymorphs) and re-precipitation of the more stable phase [49]. This implies in the case of TiO_2, that amorphous TiO_2 formed upon hydrolysis of the Ti precursor would go re-dissolution and re-crystallization to achieve amorphous to anatase phase transition, which has been evidenced in the work done by Ayral and coll. [18,19].

Based on hydrolysis-polycondensation mechanisms in sol-gel process [50], we hypothesized a mechanism for our particular sol-gel synthesis underlying the aging duration-dependent TiO_2 crystal growth as follows: as water with a relatively high H_2O/Ti molar ratio was added into the TTIP/isopropanol solution, TTIP was hydrolyzed immediately before the formed $Ti(OR)_{n-x}(OH)_x$ started quickly to condense for forming the initial Ti-O-Ti network, observed as a white precipitate (polymerization form of $Ti(OR)_{n-x}(OH)_x$). So normally, well dispersed small amorphous TiO_2 nanoparticles (precipitated as excess solute) should be stabilized thanks to the coordination ability and the specific adsorption of acetic acid on TiO_2 [51,52]. These very small size nanoparticles could serve as heterogeneous nucleation sites for the further crystallization. However, we hypothesized that the single use of acetic acid does not prevent those nucleation seeds from redissolution in acidic environment, and they are likely involved in a re-dissolution/re-crystallization equilibrium. This hypothesis is supported by the relatively low crystallinity of additive-free anatase TiO_2 crystals aged for 6 days, resulting probably from the non-stability of nucleation seeds which prevents the formation of better crystallized crystals in a limited time. A lack of solute should not be a cause here, since the reaction medium is saturated by continuously-formed TiO_2 solute during the course of the aging period. Compared to studies reported above [18,19,47–49], in which lower crystallinity TiO_2 materials were synthesized, we might propose that no better crystallized anatase TiO_2 nanocrystals might be obtained thanks to only acetic acid and an appropriate aging duration at room temperature.

A schematic illustration of the room temperature crystallization mechanism of TiO_2 in the absence of IL and additives during the aging step is presented in Fig. 9 (top):

A Initial condensation to form polymerized Ti-O-Ti chains;
B Those chains could go re-dissolution to form smaller size segments of chains in acidic condition;
C Seeds of nucleation could be formed by ordered arrangement of those small segments;
D If those seeds are stabilized, crystallization can occur from the seeds by re-arranging the rest of small chains in an ordered manner to minimize energy.

In most of the cases for TiO_2 synthesized *via* a traditional sol-gel route, the calcination-induced phase transformation comes along with a brutal crystal size increase and a sharply diminished porosity. Here, as a longer aging duration usually leads to more crystallized materials already before calcination, it might be expected that the longer-aged samples would exhibit a lower crystal size increase during the calcination step, since the already crystallized materials do not grow the way that the amorphous materials do. This contributed to the superior resistance against calcination in terms of crystal size growth shown by the longer-aged samples. This size advantage can have a very important influence on the photocatalytic activity of the sample, as small crystals provide a higher specific surface area, while a better crystallinity provides less crystal defects which are often considered as acting as charge recombination centers.

It was worth noting that the use of $BmimPF_6$ or of P-containing additive boosted the crystallization rate during aging, resulting in a better TiO_2 crystallinity compared to the TiO_2 sample synthesized without any additive before calcination. The way that phosphorous might have taken actions on size modifications of TiO_2 nanocrystals during the aging step will be detailed below.

5.2. Effect of F on TiO_2 properties and photocatalytic behavior

The TEM images of the TiO_2 photocatalysts synthesized with $BmimPF_6$ after calcination showed a unique shape evolution with the increasing aging duration. Also, TEM analysis on dried PANaF-assisted TiO_2 samples aged for 6 days (Fig. 8) showed a spindle-like shape of the nanocrystals. Although the crystals did not show the mostly reported capped bi-pyramid crystal shape obtained in many papers [37,38,45,53–57], the capping ability of F^- on exposing {001} facet is not limited only to form flat "bi-pyramid" TiO_2 crystals. It was reported that the etching chemistry of F^- on TiO_2 depends on many parameters

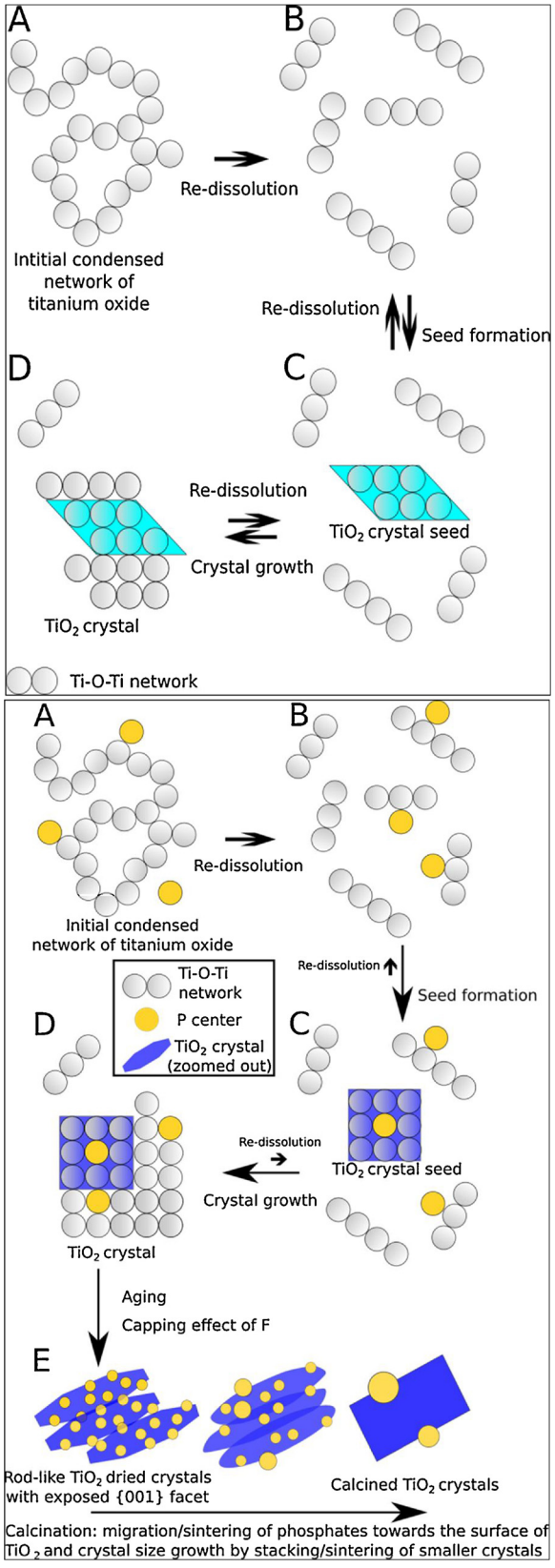

Fig. 9. Schematic illustration of the room temperature crystallization mechanism of TiO_2 without any additives (top) or with P- and F-containing additives (bottom) during aging. Note that this schema does not represent the atoms and their arrangement, but is rather conceptual and represents small size tridimensional Ti-O-Ti chains for the titanium oxide network.

such as the concentration of the capping agent or both duration and temperature of the aging [28,53,58]. *E.g.* Zhang et al. [58] have obtained rod-like anatase crystals instead of bipyramid sheet-like crystals in HF solution at 180 °C at relative higher pH values. Also, Yu et al. [59] have shown that a large quantity of $BmimBF_4$ resulted in the formation of spindle-like TiO_2 crystals, while a lower quantity led to the typical capped bi-pyramid shape. Therefore, at room-temperature and atmospheric pressure, it might be expected that the action mode of F^- on the control of the TiO_2 crystal growth and shape are much different than in hydrothermal conditions. To our knowledge, crystal shape control on TiO_2 anatase crystal by using F-derived capping agent in a mild condition has never been reported, so that great difficulty might be expected when comparing our TiO_2 crystal morphology to that demonstrated in many papers.

The PF_6^- anions of the $BmimPF_6$ ionic liquid is the only source of F available. It has been reported that the hydrolysis of $BmimPF_6$ into phosphates anions and HF can take place in acidic solution [29,60]. In our case, traces of F have been observed by XPS in TiO_2 before calcination when $BmimPF_6$ is used, as a clue that the PF_6^- ion could be hydrolyzed into phosphate and fluoride ions in our acidic reaction medium (pH around 3–4).

The exposed {001} facets of anatase TiO_2 crystals resulting from the capping effect of F^- are hypothesized to increase the photocatalytic mineralization of MEK thanks to a favored adsorption of certain VOC molecules [61]. Although we did not find studies on preferential adsorption of MEK on different anatase crystal facets, studies reported on the favored dissociative adsorption of methanol [62] and formaldehyde [63,64] on the {001} facet by using density functional theory (DFT) calculations. These molecules were not detected as intermediate products in the photocatalytic degradation of MEK in the present study, but there are chemical similarities between formaldehyde and acetaldehyde, the main detected intermediate by-product, so that we hypothesized that a higher percentage of exposed {001} facet would result in a higher acetaldehyde adsorption rate, and therefore in a higher probability for performing a full mineralization of MEK into CO_2. This may explain the increase in the CO_2 selectivity associated to the increase in the aging duration for the $BmimPF_6$- or F-assisted TiO_2 photocatalysts.

In addition, we cannot rule out a beneficial effect of exposing {001} facets on the conversion, as the recombination of photogenerated electrons and holes was reported to be lowered by spatial separation of redox sites, thanks to a selective migration of electrons and holes to specific exposed crystal faces (anisotropic electron flow) [65]. Tachikawa et al. [12] have used a single-molecule, single-particle fluorescence approach to propose that the oxidation reaction mainly occurs on the {001} facets, while the reduction reaction would mainly occur on the {101} facets. In fact, this anisotropic photogenerated electron flow has been predicted by density functional theory (DFT) calculations with the conduction band potential of anatase (101) being slightly lower than that of anatase (001) [66]. However, a too large ratio between the {001} and {101} exposed planes could decrease the photocatalytic activity due to an unbalanced oxidation-reduction site number [67]. In our case, it could not be ruled out that anatase TiO_2 crystals with enlarged but not over-exposed {001} facets could also enhance the overall oxidation of MEK, by reducing the charge recombination.

5.3. *Effect of P on TiO_2 properties and photocatalytic behavior*

To investigate the role of P in P-modified TiO_2 samples, a high P/Ti ratio up to 0.4 has been applied for the synthesis of TiO_2 with PANaF additive. According to XRD analysis, by contrast to its counterpart sample when a P/Ti molar ratio of 0.03 was used, the crystallization was strongly inhibited at 550 °C (Fig. SI 6), whereas a calcination at 800 °C (Fig. 10 top) allowed the crystallization of new titanium phosphate phases in addition to anatase, with the appearance of additional sharp peaks corresponding to both $Ti_4P_6O_{23}$ (JCPDS 039-0004) and

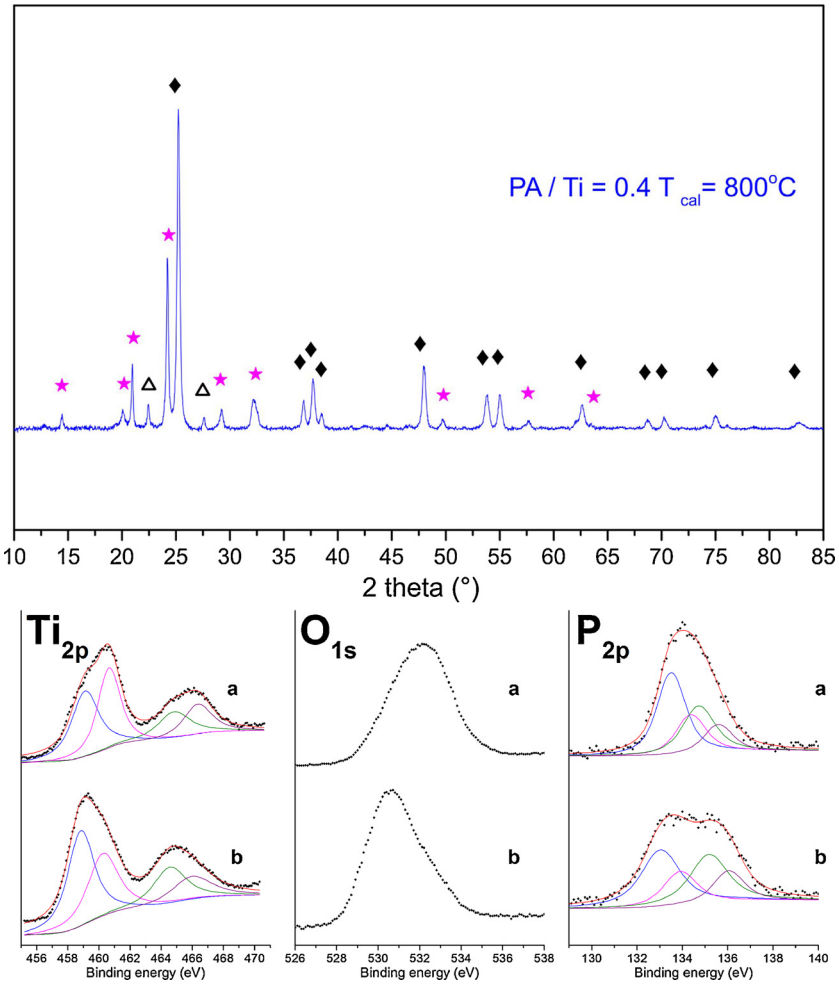

Fig. 10. (Top) XRD pattern of PANaF-TiO_2 synthesized with a PA/Ti ratio of 0.4 and a calcination temperature of 800 °C (the NaF/Ti ratio was fixed at 0.03). Black diamonds are anatase phase, magenta stars are $Ti_4P_6O_{23}$ phase, and hollow triangles are TiP_2O_7 phase. (Bottom) Ti_{2p}, O_{1s} and P_{2p} XPS patterns of PANaF-TiO_2 synthesized with a P/Ti ratio equal to 0.4 : (a) dried sample; (b) sample after calcination at 550 °C.

TiP_2O_7 (JCPDS 038–1468) phases. The presence of P and Ti-phosphate bond within the TiO_2 sample was thus revealed.

The Ti_{2p}, O_{1s} and P_{2p} XPS spectra recorded on this sample before and after calcination at 550 °C (Fig. 10 bottom) strongly differed from those recorded on the TiO_2 counterpart synthesized at the low P/Ti ratio of 0.03. Two major changes have been observed in Ti_{2p} spectra. Firstly, the Ti^{4+}-O contribution was slightly shifted to higher binding energy at *ca.* 459.1 and 464.8 eV when compared to that of P-low or P-free samples (about 0.6 eV). Secondly, in addition to the characteristic Ti^{4+}-O doublet, the Ti_{2p} spectra displayed the appearance of an additional higher energy doublet at about 460.5 and 466.2 eV. Yu et al. attributed this second additional peak to Ti^{4+} in a tetrahedral environment, indicating possible Ti-O-P bonds in titanium phosphate phase [40]. The binding energy shift value between the Ti-O-P and the Ti^{4+}-O peak in our results excided by that of the work of Yu (1.5 eV higher *vs* 0.9 eV in Yu et al.). Along with a higher peak intensity of the second doublet, such differences could result from the use of an even higher P/Ti ratio when compared to that used in Yu et al. (0.4 *vs.* 0.1). The strong increase in the O_{1s} peak area with change of the envelope profile was attributed to extra oxygen brought by phosphates as the calculated O/Ti surface atomic ratio increased up to 4.5–4.8, in agreement with studies in which PA was used during sol-gel syntheses of TiO_2 [40,68,69]. The P_{2p} spectra showed also an additional doublet contribution at about 135.0 and 135.9 eV beside the contribution corresponding to P^{5+} of usual phosphate group at 133.5 and 134.4 eV. This additional P-related doublet peak was rarely described in the literature of P-derived TiO_2 till now. Zhao et al. [68] have noticed a new $P_{2p}3/2$ contribution at 134.5 eV for PO_4^{3-}-treated TiO_2, assigned to PO_4^{3-} species bonded by bidentate form (bi-phosphate). Works of Gasik et al. [70], and Lyakishev et al. [71] have assigned new P_{2p} contributions at 135.8 eV to P within island, ring-shaped and chain-like orthophosphates or diorthophosphate motives (complex polyphosphate like $[P_3O_9]^{3-}$, $[P_2O_7]^{4-}$ and $[P_3O_{10}]^{5-}$) connected to central transition metal atoms, in their cases with manganese. Along with other groups, they have reported that the relatively high binding energy value of the polyphosphate-metal center bond resulted from the strong transfer of electron density between the P atom in the complex phosphate form, and the 3*d* transition metal central atom.

So, we preferred to hypothesize that two types of P chemical environment might exist in the TiO_2 sample synthesized with a high P/Ti ratio. The first one could consist of dispersed phosphates in TiO_2 environment, which has resulted in a higher binding energy shift of the Ti^{4+}-O doublet. The second contribution consists of a large-size titanium phosphate phase zone embedded in TiO_2 matrix, which results from the agglomeration of polymerized phosphate chains with Ti centers.

Even when a low P/Ti ratio of 0.03 was used with a resulting bulk P/Ti ratio of 0.01, for which phosphate species were finely dispersed after calcination at 550 °C and thus could not be observed *via* XRD, the electronic chemical state of Ti centers is still expected to be influenced by the presence of the phosphates within the TiO_2 crystallites. Considering that, we would like to propose a complete mechanism of P

action in P-modified TiO_2 samples.

5.3.1. Mechanism of P action with $BmimPF_6$ as P source

Since the beginning of the aging process, the partially released phosphate and the F^- ions from $BmimPF_6$ were present in the reaction medium along with the $(Ti(OR)_{n-x}(OH)_x)$ hydrolyzed titanium precursor species. The F- ions usually do not have the chelating ability to bind to more than one Ti atom. So, because of the strong interaction and high affinity between Ti centers and phosphates, the titanium phosphate precipitation was formed immediately upon contact of just-released phosphates with the titanium precursor prior to the formation of a Ti-O-Ti network, no matter the amount of P. Ti-phosphate bond is very stable, and was shown to resist to high temperature treatment [72]. We think that it is less probable for such a stable material to undergo re-dissolution in an acidic medium like it was described early. So, the aforementioned re-dissolution/re-crystallization equilibrium for the condensed Ti-O-P-O-Ti network is shifted towards re-crystallization through the presence of phosphorous. In another way to say, if the condensed Ti-O-P-O-Ti polymers serve as nucleation centers for further crystal growth, the suppression of the re-dissolution direction favors the stability of the future nucleation sites.

We propose that in the early stage of the aging step, a large number of Ti centers and phosphates reacted to form a large number of Ti-O-P-O-Ti clusters with the help of acetic acid, and those future nucleation centers were preserved in number, because of their superior stability. The room temperature crystallization of anatase crystals further carried on during aging. Note that the mean crystal size of P-involved TiO_2 samples (e.g. PANaF-derived TiO_2) did not significantly grow during the aging step. This suggests that the initial crystallization of Ti-O-P-O-Ti already occurred after 18 h (even if partially). Provided that the raw Ti material quantity was similar at the beginning of the crystallization whatever the synthesis condition, a larger number of P-involved stable nucleation centers result in a smaller final crystallized crystal size compared to the synthesis without any P-containing additives.

5.3.2. Mechanism of P action with PA as P source

The action mode and the influence of P on the TiO_2 crystal growth is believed to be similar when using PA instead of $BmimPF_6$. The main difference is that the whole amount of phosphate ions could be available earlier in the synthesis media at the beginning of the crystallization process in the case of PA, since hydrolysis of $BmimPF_6$ is needed prior to the release of phosphates when $BmimPF_6$ is used. This is thought to be in favor of a faster formation and an earlier stabilization of the Ti-O-P-O-Ti nucleation centers, that might consequently lead to a better final crystallization of TiO_2 nanocrystals. Fig. 9 (bottom) summarizes the proposed room temperature crystallization mechanism of TiO_2 in the presence of $BmimPF_6$ or P/F-containing additives during the aging step. In the following sections, the effects of this P-induced advantage will be segmented in a detailed way.

5.3.3. P-induced thermal resistance for TiO_2 photocatalysts

We have proposed that phosphorous provided thermal resistance to the materials during the calcination even when the P content is low. Unusual crystal shape- and size-change during calcination were noticed for the “PANaF 6d” sample. Spindle/rod-like nanocrystals were visualized by TEM images before calcination, with a mean length near 10 nm and a mean width around 3–4 nm, while after calcination, the crystals changed of morphology to a larger spherical shape with a mean diameter around 12 nm. We can note that the crystal growth upon calcination mainly occurred in terms of width, rather than of length. Since the crystallinity of the crystals before calcination was already rather good, the crystal width increases unlikely through the conversion of amorphous phase into crystallized TiO_2. We propose thus that the crystal growth during calcination may be caused by the sintering of already-crystallized crystals along the length in direction. As example, this means that a final spherical TiO_2 crystal with a diameter of 12 nm could schematically result from the sintering of three rod-like-shape crystals stacked together along their length direction during calcination.

This P-induced limited crystal size growth mechanism is responsible for the smaller crystal size and the larger specific surface area of such TiO_2 photocatalysts compared to the P-free TiO_2 materials after calcination. We hypothesized that this behavior is responsible for the enhancement of the MEK conversion rate due to the exposure of more adsorption sites. The limitation of the crystal size growth during the $BmimPF_6$ ionic liquid template-based sol-gel synthesis of TiO_2 was already reported, but no explanation was proposed till now [26,27]. According to us, this is the most important feature brought by P in terms of boosting the photocatalytic activity of TiO_2. However, we cannot rule out a direct positive effect of negatively-charged phosphate anions on the photocatalytic activity, since they have been already reported being capable to attract photogenerated holes, thus preventing electron-hole recombination [68].

6. Conclusion

Highly crystallized anatase TiO_2 nanoparticles were prepared with crystallite size and shape control *via* a $BmimPF_6$ ionic liquid or PA/NaF assisted sol-gel synthesis. We showed that $BmimPF_6$ ionic liquid could be efficiently substituted by cheap PA and NaF additives in an adequate ratio in the sol-gel synthesis for synthesizing TiO_2 photocatalysts without altering the main physico-chemical properties and the photocatalytic activity. We proposed a correlation between the main bulk and surface physico-chemical properties and the photocatalytic activity of the TiO_2 materials, and highlighted a similar combined role of phosphate and fluoride ions, whether they are brought by the $BmimPF_6$ ionic liquid or by the PA and NaF additives. When synthesized with an extended aging time, TiO_2 synthesized in the presence of phosphate and fluoride ions displayed a higher MEK conversion and a twice higher mineralization yield in the gas phase degradation of MEK under UVA light, in comparison to the TiO_2 Aeroxide P25 reference and the sol-gel TiO_2 counterpart synthesized in the absence $BmimPF_6$.

In both cases, the reaction of phosphates with the titanium hydroxide network in the early stage of the sol-gel synthesis was proposed to result in a size control of TiO_2 crystallites and thus in a higher specific surface area, in favor of a higher MEK conversion rate, while the fluoride ions were proposed to cause an anisotropic TiO_2 crystal growth during the aging step of the sol gel synthesis, in favor of a higher selectivity to CO_2 through a favored adsorption of intermediate products of MEK degradation on the exposed TiO_2 {001} facets.

Acknowledgements

This work is part of the CLEANCOAT project funded by the CARNOT MICA (Materials Institute Carnot Alsace). A. Rach and M. Wolf (ICPEES) are thanked for their contributions on the photocatalytic test setup. P. Bernhardt and V. Papaefthymiou (ICPEES) are acknowledged for XPS measurements. L. Vidal (IS2M) is thanked for performing TEM analysis.

Appendix A. Supplementary data

Supplementary material related to this article can be found, in the online version, at doi:https://doi.org/10.1016/j.apcatb.2018.04.027.

References

[1] M.R. Hoffmann, S.T. Martin, W.Y. Choi, D.W. Bahnemann, Environmental applications of semiconductor photocatalysis, Chem. Rev. 95 (1995) 69–96.
[2] M. Anpo, M. Takeuchi, The design and development of highly reactive titanium oxide photocatalysts operating under visible light irradiation, J. Catal. 216 (2003) 505–516.
[3] A. Enesca, Y. Yamaguchi, C. Terashima, A. Fujishima, K. Nakata, A. Duta, Enhanced uv-vis photocatalytic performance of the $CuInS_2/TiO_2/SnO_2$ hetero-structure for air

decontamination, J. Catal. 350 (2017) 174–181.
[4] N.N. Lichtin, M. Avudaithai, E. Berman, J. Dong, Photocatalytic oxidative degradation of vapors of some organic compounds over TiO_2, Res. Chem. Intermed. 20 (1994) 755–781.
[5] C.S. Turchi, D.F. Ollis, Photocatalytic degradation of organic water contaminants: mechanisms involving hydroxyl radical attack, J. Catal. 122 (1990) 178–192.
[6] J. Zhao, X. Yang, Photocatalytic oxidation for indoor air purification: a literature review, Build. Environ. 38 (2003) 645–654.
[7] M. Pelaez, N.T. Nolan, S.C. Pillai, M.K. Seery, P. Falaras, A.G. Kontos, P.S.M. Dunlop, J.W.J. Hamilton, J.A. Byrne, K. O'Shea, M.H. Entezari, D.D. Dionysiou, A review on the visible light active titanium dioxide photocatalysts for environmental applications, Appl. Catal. B: Environ. 125 (2012) 331–349.
[8] A. Alonso Tellez, R. Masson, D. Robert, N. Keller, V. Keller, Comparison of Hombikat UV100 and P25 TiO_2 performance in gas-phase photocatalytic oxidation reactions, J. Photochem. Photobiol. A Chem. 250 (2012) 58–65.
[9] G. Lu, A. Linsebigler, J.T. Yates Jr, Ti^{3+} defect sites on TiO_2 (110): production and chemical detection of active sites, J. Phys. Chem. 98 (1994) 11733–11738.
[10] N. Keller, E. Barraud, F. Bosc, D. Edwards, V. Keller, On the modification of photocatalysts for improving visible light and UV degradation of gas-phase toluene over TiO_2, Appl. Catal. B: Environ. 70 (2007) 423–430.
[11] S.W. Verbruggen, K. Masschaele, E. Moortgat, T.E. Korany, B. Hauchecorne, J.A. Martens, S. Lenaerts, Factors driving the activity of commercial titanium dioxide powders towards gas phase photocatalytic oxidation of acetaldehyde, Catal. Sci. Technol. 2 (2012) 2311.
[12] T. Tachikawa, S. Yamashita, T. Majima, Evidence for crystal-face-dependent TiO_2 photocatalysis from single-molecule imaging and kinetic analysis, J. Am. Chem. Soc. 133 (2011) 7197–7204.
[13] L.L. Hench, S.H. Wang, The sol-gel glass transformation of silica, Phase Transit. 24-6 (1990) 785–834.
[14] Y. Wang, Y. He, Q. Lai, M. Fan, Review of the progress in preparing nano TiO_2: an important environmental engineering material, J. Environ. Sci. (China) 26 (2014) 2139–2177.
[15] V. Loryuenyong, K. Angamnuaysiri, J. Sukcharoenpong, A. Suwannasri, Sol–gel derived mesoporous titania nanoparticles: effects of calcination temperature and alcoholic solvent on the photocatalytic behavior, Ceram. Int. 38 (2012) 2233–2237.
[16] K.A. Malinger, A. Maguer, A. Thorel, A. Gaunand, J.F. Hochepied, Crystallization of anatase nanoparticles from amorphous precipitate by a continuous hydrothermal process, Chem. Eng. J. 174 (2011) 445–451.
[17] M. Grandcolas, M. Karkmaz Le Du, F. Bosc, A. Louvet, N. Keller, V. Keller, Porogen template assisted TiO_2 rutile coupled nanomaterials for improved visible and solar light photocatalytic applications, Catal. Lett. 123 (2008) 65–71.
[18] F. Bosc, A. Ayral, P.A. Albouy, C. Guizard, A simple route for low-temperature synthesis of mesoporous and nanocrystalline anatase thin films, Chem. Mater. 15 (2003) 2463–2468.
[19] F. Bosc, A. Ayral, P.A. Albouy, L. Datas, C. Guizard, Mesostructure of anatase thin films prepared by mesophase templating, Chem. Mater. 16 (2004) 2208–2214.
[20] Y. Wang, S. Maksimuk, R. Shen, H. Yang, Synthesis of iron oxide nanoparticles using a freshly-made or recycled imidazolium-based ionic liquid, Green Chem. 9 (2007) 1051.
[21] Z. Xie, M. Feng, B. Tan, X. Huang, The multifunctional roles of the ionic liquid [Bmim][BF_4] in the creation of cadmium metal–organic frameworks, CrystEngComm 14 (2012) 4894.
[22] A. Vioux, L. Viau, S. Volland, J. Le Bideau, Use of ionic liquids in sol-gel: ionogels and applications, Comptes Rendus Chimie 13 (2010) 242–255.
[23] F. Endres, Ionic liquids: solvents for the electrodeposition of metals and semiconductors, ChemPhysChem 3 (2002) 144–154.
[24] H. Zhu, J. Huang, Z. Pan, S. Dai, Ionothermal synthesis of hierarchical ZnO nanostructures from ionic-liquid precursors, Chem. Mater. 18 (2006) 4473–4477.
[25] C.M. Lee, H.J. Jeong, S.T. Lim, M.H. Sohn, D.W. Kim, Synthesis of iron oxide nanoparticles with control over shape using imidazolium-based ionic liquids, ACS Appl. Mater. Interfaces 2 (2010) 756–759.
[26] K.S. Yoo, T.G. Lee, J. Kim, Preparation and characterization of mesoporous TiO_2 particles by modified sol–gel method using ionic liquids, Microporous Mesoporous Mater. 84 (2005) 211–217.
[27] E.H. Choi, S.I. Hong, D.J. Moon, Preparation of thermally stable mesostructured nano-sized TiO_2 particles by modified sol–gel method using ionic liquid, Catal. Lett. 123 (2008) 84–89.
[28] X.W. Zhao, W.Z. Jin, J.G. Cai, J.F. Ye, Z.H. Li, Y.R. Ma, J.L. Xie, L.M. Qi, Shape- and size-controlled synthesis of uniform anatase TiO_2 nanocuboids enclosed by active {100} and {001} facets, Adv. Funct. Mater. 21 (2011) 3554–3563.
[29] M.G. Freire, C.M.S.S. Neves, I.M. Marrucho, J.A.P. Coutinho, M. Fernandes, Hydrolysis of tetrafluoroborate and hexafluorophosphate counter ions in imidazolium-based ionic liquids, J. Phys. Chem. A 114 (2010) 3744–3749.
[30] C. Raillard, V. Héquet, P.L. Cloirec, J. Legrand, TiO_2 coating types influencing the role of water vapor on the photocatalytic oxidation of methyl ethyl ketone in the gas phase, Appl. Catal. B: Environ. 59 (2005) 213–220.
[31] G. Vincent, A. Queffeulou, P.M. Marquaire, O. Zahraa, Remediation of olfactory pollution by photocatalytic degradation process: study of methyl ethyl ketone (MEK), J. Photochem. Photobiol. A Chem. 191 (2007) 42–50.
[32] G. Vincent, P.M. Marquaire, O. Zahraa, Abatement of volatile organic compounds using an annular photocatalytic reactor: study of gaseous acetone, J. Photochem. Photobiol. A Chem. 197 (2008) 177–189.
[33] M.H. Jung, M.J. Chu, M.G. Kang, TiO2 nanotube fabrication with highly exposed (001) facets for enhanced conversion efficiency of solar cells, Chem. Commun. 48 (2012) 5016–5018.
[34] ISO, Fine Ceramics (Advanced Ceramics, Advanced Technical Ceramics) – Test Method for Air-Purification Performance of Semiconducting Photocatalytic Materials – Part 2: Removal of Acetaldehyde, Fine Ceramics (Advanced Ceramics, Advanced Technical Ceramics) – Test Method for Air-Purification Performance of Semiconducting Photocatalytic Materials 22197-2, (2011).
[35] R. Masson, V. Keller, N. Keller, β-SiC alveolar foams as a structured photocatalytic support for the gas phase photocatalytic degradation of methylethylketone, Appl. Catal. B: Environ. 170-171 (2015) 301–311.
[36] Y. Liao, H. Zhang, W. Que, P. Zhong, F. Bai, Z. Zhong, Q. Wen, W. Chen, Activating the single-crystal TiO2 nanoparticle film with exposed {001} facets, ACS Appl. Mater. Interfaces 5 (2013) 6463–6466.
[37] H. Yang, C. Sun, S. Qiao, J. Zou, G. Liu, S. Smith, H. Cheng, G. Lu, Anatase TiO_2 single crystals with a large percentage of reactive facets, Nature 453 (2008) 638–641.
[38] X. Yang, Z. Li, C. Sun, H. Yang, C. Li, Hydrothermal stability of {001} faceted anatase TiO_2, Chem. Mater. 23 (2011) 3486–3494.
[39] A.A.S. Alfaya, Y. Gushikem, S.C. de Castro, Highly dispersed phosphate supported in a binary silica-titania matrix: preparation and characterization, Chem. Mater. 10 (1998) 909–913.
[40] J.C. Yu, L. Zhang, Z. Zheng, J. Zhao, Synthesis and characterization of phosphated mesoporous tianium dioxide with high photocatalytic activity, Chem. Mater. 15 (2003) 2280–2286.
[41] S.J. Splinter, R. Rofagha, N.S. McIntyre, U. Erb, XPS characterization of the corrosion films formed on nanocrystalline ni-p alloys in sulphuric acid, Surf. Interface Anal. 24 (1996) 181–186.
[42] A.I. Bortun, S.A. Khainakov, L.N. Bortun, D.M. Poojary, J. Rodriguez, J.R. Garcia, A. Clearfield, Synthesis and characterization of two novel fibrous titanium phosphates $Ti_2O(PO_4)_2.2H_2O$, Chem. Mater. 9 (1997) 1805–1811.
[43] V. Sudarsan, K.P. Muthe, J.C. Vyas, S.K. Kulshreshtha, PO_4^{3-} tetrahedra in $SbPO_4$ and $SbOPO_4$: a 31P NMR and XPS study, J. Alloys Compd. 336 (2002) 119–123.
[44] K. Elghniji, M.E. Saad, M. Araissi, E. Elaloui, Y. Moussaoui, Chemical modification of TiO_2 by $H_2PO_4^-$/HPO_4^{2-} anions using the sol-gel route with controlled precipitation and hydrolysis: enhancing thermal stability, Mater. Sci. 32 (2014) 617–625.
[45] S. Liu, J. Yu, B. Cheng, M. Jaroniec, Fluorinated semiconductor photocatalysts: tunable synthesis and unique properties, Adv. Colloid Interface Sci. 173 (2012) 35–53.
[46] D.C. Hurum, A.G. Agrios, K.A. Gray, T. Rajh, M.C. Thurnauer, Explaining the enhanced photocatalytic activity of degussa P25 mixed-phase TiO_2 using EPR, J. Phys. Chem. B 107 (2003) 4545–4549.
[47] D.S. Seo, J.K. Lee, E.G. Lee, H. Kim, Effect of aging agents on the formation of TiO_2 nanocrystalline powder, Mater. Lett. 51 (2001) 115–119.
[48] K. Qi, J. Xin, Room-temperature synthesis of single-phase anatase TiO_2 by aging and its self-cleaning properties, ACS Appl. Mater. Interfaces 2 (2010) 3479–3485.
[49] Q. Zhang, S. Liu, S. Yu, Recent advances in oriented attachment growth and synthesis of functional materials: concept, evidence, mechanism, and future, J. Mater. Chem. 19 (2009) 191–207.
[50] C. Su, B.Y. Hong, C.M. Tseng, Sol–gel preparation and photocatalysis of titanium dioxide, Catal. Today 96 (2004) 119–126.
[51] J. Livage, Sol-gel synthesis of heterogeneous catalysts from aqueous solutions, Catal. Today 41 (1998) 19.
[52] J. Polleux, N. Pinna, M. Antonietti, C. Hess, U. Wild, R. Schlögl, M. Niederberger, Ligand functionality as a versatile tool to control the assembly behavior of preformed titania nanocrystals, Chem. A Eur. J. 11 (2005) 3541–3551.
[53] C. Chen, R. Hu, K. Mai, Z. Ren, H. Wang, G. Qian, Z. Wang, Shape evolution of highly crystalline anatase TiO_2 nanobipyramids, Cryst. Growth Des. 11 (2011) 5221–5226.
[54] F. Tian, Y. Zhang, J. Zhang, C. Pan, Raman spectroscopy: a new approach to measure the percentage of anatase TiO_2 exposed (001) facets, J. Phys. Chem. C 116 (2012) 7515–7519.
[55] M.V. Sofianou, V. Psycharis, N. Boukos, T. Vaimakis, J. Yu, R. Dillert, D. Bahnemann, C. Trapalis, Tuning the photocatalytic selectivity of TiO_2 anatase nanoplates by altering the exposed crystal facets content, Appl. Catal. B: Environ. 142-143 (2013) 761–768.
[56] Y. Wang, H. Sun, S. Tan, H. Feng, Z. Cheng, J. Zhao, A. Zhao, B. Wang, Y. Luo, J. Yang, J.G. Hou, Role of point defects on the reactivity of reconstructed anatase titanium dioxide (001) surface, Nat. Commun. 4 (2013) 2214.
[57] Y. Luan, L. Jing, J. Wu, M. Xie, Y. Feng, Long-lived photogenerated charge carriers of 001-facet-exposed TiO_2 with enhanced thermal stability as an efficient photocatalyst, Appl. Catal. B: Environ. 147 (2014) 29–34.
[58] H. Zhang, Y. Wang, P. Liu, Y. Han, X. Yao, J. Zou, H. Cheng, H. Zhao, Anatase TiO_2 crystal facet growth: mechanistic role of hydrofluoric acid and photoelectrocatalytic activity, ACS Appl. Mater. Interfaces 3 (2011) 2472–2478.
[59] S. Yu, B. Liu, Q. Wang, Y. Gao, Y. Shi, X. Feng, X. An, L. Liu, J. Zhang, Ionic liquid assisted chemical strategy to TiO_2 hollow nanocube assemblies with surface-fluorination and nitridation and high energy crystal facet exposure for enhanced photocatalysis, ACS Appl. Mater. Interfaces 6 (2014) 10283–10295.
[60] R.P. Swatloski, J.D. Holbrey, R.D. Rogers, Ionic liquids are not always green: hydrolysis of 1-butyl-3-methylimidazolium hexafluorophosphate, Green Chem. 5 (2003) 361.
[61] K. Lv, B. Cheng, J. Yu, G. Liu, Fluorine ions-mediated morphology control of anatase TiO_2 with enhanced photocatalytic activity, Phys. Chemistry Chemical Phys.: PCCP 14 (2012) 5349–5362.
[62] W. Fang, X. Gong, H. Yang, On the unusual properties of anatase TiO_2 exposed by highly reactive facets, J. Phys. Chem. Lett. 2 (2011) 725–734.
[63] P. Zhou, X. Zhu, J. Yu, W. Xiao, Effects of adsorbed F, OH, and Cl ions on formaldehyde adsorption performance and mechanism of anatase TiO_2 nanosheets

with exposed {001} facets, ACS Appl. Mater. Interfaces 5 (2013) 8165–8172.
[64] H. Liu, X. Wang, C. Pan, K.M. Liew, First-principles study of formaldehyde adsorption on TiO_2 rutile (110) and anatase (001) surfaces, J. Phys. Chem. C 116 (2012) 8044–8053.
[65] N. Murakami, Y. Kurihara, T. Tsubota, T. Ohno, Shape-controlled anatase titanium (IV) oxide particles prepared by hydrothermal treatment of peroxo titanic acid in the presence of polyvinyl alcohol, J. Phys. Chem. C 113 (2009) 3062–3069.
[66] Y. Li, Z. Liu, L. Liu, W. Gao, Mechanism and activity of photocatalytic oxygen evolution on titania anatase in aqueous surroundings, J. Am. Chem. Soc. 132 (2010) 13008–13015.
[67] Q. Xiang, K. Lv, J. Yu, Pivotal role of fluorine in enhanced photocatalytic activity of anatase TiO_2 nanosheets with dominant (001) facets for the photocatalytic degradation of acetone in air, Appl. Catal. B: Environ. 96 (2010) 557–564.
[68] D. Zhao, C. Chen, Y. Wang, H. Ji, W. Ma, L. Zang, J. Zhao, Surface modification of TiO_2 by phosphate: effect on photocatalytic activity and mechanism implication, J. Phys. Chem. C 112 (2008) 5993–6001.
[69] L. Korosi, A. Oszko, G. Galbacs, A. Richardt, V. Zollmer, I. Dekany, Structural properties and photocatalytic behaviour of phosphate-modified nanocrystalline titania films, Appl. Catal. B: Environ. 77 (2007) 175–183.
[70] M. Gasik, V. Gladkikh, The investigation of phosphorus chemical bond in the manganese-ore materials, The Fourteenth International Ferroalloys Congress, Kiev, Ukraine, (May 31-June 4, 2015), 2015, pp. 470–478.
[71] N.P. Lyakishev, V.A. Gladkikh, M.I. Gasik, The nature of chemical bonding of phosphorus in monomineral fractions and concentrates of manganese ores, Russ. Metall. (1994) 1–9.
[72] A. Bhaumik, S. Inagaki, Mesoporous titanium phosphate molecular sieves with ion-exchange capacity, J. Am. Chem. Soc. 123 (2001) 691–696.